https://doi.org/10.5194/egusphere-2026-2351
Preprint. Discussion started: 20 May 2026

Evaluating stable isotopic compositions in near-surface atmospheric water vapor over the Tibetan Plateau using the isotope-enabled atmospheric general circulation model ECHAM6-wiso

Yigang Liu[1,2], Jing Gao[1*], Martin Werner[3], Alexandre Cauquoin[4], Ke Li[1,2]

[1]State Key Laboratory of Tibetan Plateau Earth System, Environment and Resources (TPESER), Institute of Tibetan Plateau Research, Chinese Academy of Sciences, Beijing 100101, China

[2]University of Chinese Academy of Sciences, Beijing 100049, China

[3]Alfred Wegener Institute (AWI), Helmholtz Centre for Polar and Marine Sciences, Bremerhaven, Germany

[4]Institute of Industrial Science (IIS), The University of Tokyo, Kashiwa, Japan

Corresponding author: Jing Gao (gaojing@itpcas.ac.cn)

https://doi.org/10.5194/egusphere-2026-2351
Preprint. Discussion started: 20 May 2026

Abstract. Water stable isotopologues, particularly $H_2{}^{18}O$ and $HD^{16}O$, are valuable tracers of physical and dynamical processes within the hydrological cycle. These isotopologues have been widely incorporated into isotope-enabled atmospheric general circulation models to constrain moisture sources and transport pathways. However, comprehensive evaluations of such models over the Tibetan Plateau (TP), a region whose complex orography substantially modulates South Asian monsoon dynamics, remain scarce. Here, we systematically evaluate simulations of water vapor isotopic composition ($\delta^{18}O_v$) from the ECHAM6-wiso model against daily in-situ observations from four high-altitude stations (Kathmandu, Lulang, Namco, and Muztag) on the Tibetan Plateau, spanning January 2020 to November 2021. The model successfully reproduces the spatial distribution and seasonal cycle of $\delta^{18}O_v$; however, probability density functions reveal a systematic underestimation of isotopic depletion. Through a multi-scale temporal decomposition of the daily $\delta^{18}O_v$ time series, we attribute over 50% of the simulation error to deficiencies in representing large-scale atmospheric circulations (periods ≥ 30 days), while the remaining error is linked to synoptic-scale processes (3-7 days) associated with fractionation, including cloud microphysics, post-condensation effects, and surface evaporation. The model's inability to accurately simulate terrain-induced atmospheric moisture blocking over the TP results in bias in atmospheric circulation variations, thereby amplifying the contribution of circulation-related processes to the overall error. These findings underscore the significance of atmospheric circulation in water vapor isotopic simulations and highlight the value of high-resolution water vapor isotopic datasets for improving our understanding of moisture source attribution and water-cycle dynamics in regions of complex topography.

Highlights:

1. We provide the first systematic evaluation of ECHAM6-wiso's ability to simulate water vapor isotope ratios in near-surface over the TP.
2. A systematic positive bias, specifically an underestimation of isotopic depletion is identified.
3. Our analysis reveals that low-frequency components dominate the simulation error.

https://doi.org/10.5194/egusphere-2026-2351
Preprint. Discussion started: 20 May 2026

1 Introduction

The Tibetan Plateau (TP), with an average elevation exceeding 4,000 m, is the source of many of Asia's major rivers and is often referred to as the "Asian water tower" (Xu et al., 2008; Immerzeel et al., 2010). The regional atmospheric water cycle over the TP plays a crucial role in regulating water resources through precipitation and evaporation, directly impacting water availability in downstream areas (Gao et al., 2019; Yao et al., 2022). Moisture transport processes are fundamental to this cycle, yet mechanisms governing changes in moisture pathways and source contributions remain poorly understood. (Sun et al., 2022).

Because the hydrogen and oxygen atoms have several natural isotopes, it results several forms of the water molecule called stable water isotopologues (primarily $H_2{}^{16}O$, $H_2{}^{18}O$, and $HD^{16}O$). Differences in molecular mass and symmetry lead to isotopic fractionation during phase transitions. For instance, heavier isotopologues such as $H_2{}^{18}O$ are more easily transferred to the liquid phase during condensation, compared to the lighter ones (e.g., $H_2{}^{16}O$), making these species effective passive tracers of various processes within the hydrological cycle.

The application of stable isotopologues in hydrology, expressed in the usual δ notation (e.g., $\delta^{18}O$ with respect to the Vienna Standard Mean Ocean Water V-SMOW), has a long history (Epstein & Mayeda, 1953; Dansgaard, 1954; Craig, 1961; Gat, 1996). Since 1961, the Global Network of Isotopes in Precipitation (GNIP) database, coordinated by the IAEA/WMO, has collected monthly precipitation samples for isotopic analysis worldwide. These data have revealed characteristic fractionation patterns, such as depletion along poleward transport gradients and temperature-dependent isotopic signatures (Dansgaard, 1964).

Advancements in laser absorption spectroscopy since the 1990s have enabled high-frequency *in situ* measurements of water vapor isotopic compositions (Scherer et al., 1997; Baer et al., 2002; Crosson et al., 2002). These isotopic analyzers can resolve isotope ratios at second intervals and are deployable across diverse observational platforms. For example, Kurita et al. (2011) showed water vapor isotope measurements during the Madden-Julian Oscillation (MJO) collected by a maritime campaign. More

https://doi.org/10.5194/egusphere-2026-2351
Preprint. Discussion started: 20 May 2026

recently, Finkenbiner et al. (2022) published an open-access dataset of water vapor isotope profiles from flux towers across the United States, and Sarkar et al. (2023) provided the isotope ratios sampled by the NOAA P3 aircraft in the North Atlantic winter trade wind region. Rapidly increasing water stable isotope measurements have greatly enhanced our understanding of water cycle, especially in aspect of large-scale circulation transport. Tan (2013) examined the significance of El Niño-Southern Oscillation (ENSO) on inter-annual variation of $\delta^{18}O$ in the monsoon regions of China and found that trade wind plays a role in governing $\delta^{18}O$ through affecting the intensity of the different summer monsoon circulations. Yao et al. (2013) revealed three distinct domains associated with influence of the westerlies and Indian summer monsoon using observed precipitation isotopes over the TP. Putman et al. (2017) linked variability in vapor source region and transport trajectory with precipitation isotopes at Utqiagvik, USA. In addition, high temporal resolution measurements also provide an efficient reference for model evaluations.

Concurrently, isotope modelling capabilities have also progressed substantially. Isotope models are typically divided into Rayleigh-type models, which are based on idealized fractionation assumptions, and isotope-enabled atmospheric general circulation models (AGCMs), which integrate isotopic tracers into fully climate dynamics governed by the Navier-Stokes equations and thermodynamics. Dansgaard (1964) proposed for the first time the classical Rayleigh fractionation model to describe isotopic evolution in air masses. Subsequent developments included kinetic fractionation effects during precipitation (Stewart, 1975), a theoretical framework for different water reservoirs (Merlivat and Jouzel 1979, hereafter called MJ79). Jouzel and Merlivat (1984) improved the Rayleigh model by considering the existence of isotopic kinetic effects during snow formation. Ciais and Jouzel (1994) proposed a one-dimensional mixed-cloud isotopic model (MCIM) to account for coexisting liquid and solid phases. However, such Rayleigh-type models remain limited in their representation of atmospheric dynamics and vertical mixing (Jouzel et al., 1987; Hoffmann, 1998).

Isotope-enabled AGCMs offer a more comprehensive framework and physically modeling results by explicitly coupling isotopic tracers into global circulation and

https://doi.org/10.5194/egusphere-2026-2351
Preprint. Discussion started: 20 May 2026

hydrological processes. Joussaume et al. (1984) pioneered the integration of isotopes into an AGCM (Laboratoire de Meteorologie Dynamique, called LMD), demonstrating the method's utility for capturing observed water isotope variations. Since then, several efforts have been made to include isotopic tracers into models. Jouzel et al. (1987) were the first to simulate seasonal isotope cycles using the GISS AGCM. Hoffmann (1998) incorporated isotopes into ECHAM3 and found that an improved representation of advection and orography is critical on the interannual timescale. Mathieu et al. (2002) introduced a more detailed parameterizations related to postcondensation processes into the GENESIS 2.0b and pointed including downdrafts and associated isotopic processes would lead to more realistic results, especially in the tropics. Sturm et al. (2005) implemented high-resolution regional simulations with $REMO_{iso}$. Lee & Fung et al. (2008) proposed a novel method that describes the interaction between raindrops and atmosphere near the planetary boundary layer to explain the "amount effect" and was applied to CAM2. Werner et al. (2010) extended isotopic resolution globally to 0.75° in ECHAM5-wiso. Haese et al. (2013) incorporated water stable isotopes in coupled atmosphere-land surface model ECHAM5-JSBACH and found that simulated $\delta^{18}O$ in precipitation at monthly and interannual time scales is only slightly affected by fractionation effects during land surface evaporation. Using the isotope-enabled land soil model Iso-MATSIRO (Yoshimura et al., 2017), Okazaki et al. (2019) showed that land surface fractionation greatly influenced daily precipitation isotopes.

Isotope-enabled AGCMs have significantly advanced our understanding of how isotopic variability reflects environmental conditions. For example, He et al. (2015) used LMDZiso to study convection influences on summer precipitation stable isotopic variability at daily resolution and found that daily precipitation stable isotopes are well correlated with upstream convective activities. Gao et al. (2011) used two isotope-enabled AGCMs (LMDZiso and ECHAM4-wiso) to examine the processes driving precipitation stable isotopic variability over the TP and found that very large systematic biases in these two AGCMs regarding the properties of water stable isotopes in precipitation. The complex topography hindered the corrected simulation of moisture advection from lowlands to the TP. At high altitudes, models simulate steeper-elevation

https://doi.org/10.5194/egusphere-2026-2351
Preprint. Discussion started: 20 May 2026

isotope than is observed. Yao et al. (2013) explored climatic controls of precipitation $\delta^{18}O$ over the TP with three isotope-enabled AGCMs (LMDZiso, REMOiso, and ECHAM5-wiso) and found that models fail to correctly simulate relationships between precipitation stable isotopes and precipitation amount in the monsoon domain. They emphasized the importance of assessment at interannual and longer timescales.

Although previous studies have conducted relatively comprehensive works on model-observation comparisons, assessments were almost focusing on precipitation stable isotopes due to limitation of observational water vapor isotopes over the TP. The reliability of models for simulated water vapor isotopes over the TP needs to be verified. Furthermore, the accuracy of simulated water vapor isotopic ratios is highly sensitive to model parameterization. Risi et al. (2010) identified two parameters governing kinetic fractionation under supersaturated conditions and relative humidity at the droplet interface are critical for water vapor isotopic simulation. Nusbaumer et al. (2016) performed a series of sensitivity experiments and found that the threshold triggering convection will greatly modulates water vapor isotopic simulations. However, the default parameter values in many isotope-enabled AGCMs are derived from datasets collected in Antarctica and Greenland (Epstein & Mayeda, 1953; Horibe and Ogura, 1968; Ohmura et al., 1991). As a result, these schemes can be inappropriate for the TP region and may introduce significant uncertainties, underscoring the need for model evaluation (and calibration) using water vapor isotopic observations on the TP.

In this study, we present the first evaluation of water vapor isotopic composition over the TP simulated by the isotope-enabled AGCM, ECHAM6-wiso (Cauquoin and Werner, 2021), using high-frequency isotope measurements during 2020-2021. Especially, after a comparison of spatiotemporal distributions of water vapor isotope ratios between simulation and observations, we apply probability-density functions to obtain a concrete and measurable understanding of isotopic simulation errors. Finally, daily $\delta^{18}O_v$ time series were decomposed using temporal domain decomposition techniques to clarify the error contributions of different time-scales processes.

2 Methods

https://doi.org/10.5194/egusphere-2026-2351
Preprint. Discussion started: 20 May 2026

2.1 Observational Data

Water vapor isotopic ratios were obtained from four high-altitude monitoring stations on the TP (Table 1, map of locations is provided in Supplementary materials). Kathmandu station is located on the southern slope of the Himalayas at approximately 1400 m a. s. l., with a mean annual temperature of 19 ℃ and annual precipitation of about 1500 mm (Adhikari et al., 2024). The Lulang station lies in a mountain valley on the northern slope of the Himalayas at an altitude of 3326 m a.s.l., with an average annual temperature of about 5 ℃ and precipitation of about 770 mm (Chen et al., 2024). The Namco station is situated near the southeast bank of Namco lake with an altitude of 4730 m a.s.l. It has an average annual temperature of 0 ℃ and receives about 281.8 mm of precipitation amount annually. The lake begins freezing in November, is fully frozen by mid to late January, and thaws completely by May. The Muztag station is located in the northwestern TP, near the Muztag Mountain at approximately 3650 m a. s. l., with a mean annual temperature of 1.1 ℃ and annual precipitation of about 119.4 mm. Seasonal cycles of temperature and precipitation at these four stations are provided in Supplementary materials.

Water vapor isotopic measurements at all sites were performed using high-frequency Picarro L2130-i Laser Spectrometers, installed near the ground surface. Standard atmospheric variables (air temperature, precipitation intensity, and specific humidity) were measured by the flexible weather stations from DAVIS. All measured data were averaged to daily and monthly resolutions to facilitate comparison with model outputs. Details of instrument calibration and quality control procedures are provided in Supplementary materials.

Due to the sparse distribution of monitoring stations over the TP, HARv2 dataset was used to examine the spatial patterns of simulated atmospheric variables. HARv2 is a regional high-resolution atmospheric dataset generated by dynamical downscaling using WRF (Wang et al., 2021).

Table 1. High-altitude monitoring stations from which Observational data was collected for comparison with ECHAM6-wiso simulation results.

https://doi.org/10.5194/egusphere-2026-2351
Preprint. Discussion started: 20 May 2026

Station	Longitude (°E)	Latitude (°N)	Altitude (m a.s.l.)	Mean annual temperature (℃)	Mean annual precipitation (mm)
Kathmandu	85.20	27.42	1400	19	1500
Lulang	94.73	29.77	3326	5	770
Namco	90.99	30.77	4730	0	281.8
Muztag	75.04	38.41	3650	1.1	119.4

2.2 ECHAM6-Wiso Model and Simulation Experiment

ECHAM6 is the sixth-generation of atmospheric general circulation model ECHAM, developed by the Max Planck Institute for Meteorology (Stevens et al., 2013). Relative to its predecessor ECHAM5, major improvements that affect the simulation of isotopic water cycle include enhanced representations of shortwave radiation and convective processes. The model employ the Tiedtke-Nordeng-Tiedtke (TNT) moist convection scheme (Tiedtke, 1989; Nordeng, 1994). Unlike ECHAM5, where the temperature excess required to trigger convection was fixed at 0.5 K, in ECHAM6 this threshold is now dynamically determined via a prognostic treatment of temperature variance within the planetary boundary layer. In addition to standard cloud microphysics, the model includes additional processes such as condensate production due to turbulent mixing. The isotope-enabled version of the model ECHAM6, ECHAM6-wiso (Cauquoin et al., 2019), was built in an analogous manner to previous ECHAM releases (Hoffmann et al., 1998; Werner et al., 2010). The “isotopic” (i.e., heavier) and “normal” (i.e., lighter) water cycle are treated identically in the model, except during phase changes, where fractionation is explicitly accounted for. Full technical details refer to Cauquoin et al. (2019).

https://doi.org/10.5194/egusphere-2026-2351
Preprint. Discussion started: 20 May 2026

Cauquoin and Werner (2021) introduced several updates to ECHAM6-wiso, including a slight modification to the supersaturation equation from $S = 1.01 - 0.0045 \cdot T_{cond}$ to $S = 1.02 - 0.0045 \cdot T_{cond}$. Isotopic composition of snow on sea ice is now included for sublimation processes in sea-ice covered regions. Kinetic fractionation factors for oceanic evaporation have been revised to be wind-speed independent. In addition, ECHAM6-wiso is now nudged to ERA5 reanalysis data, replacing the previously used ERA-Interim dataset.

In this study, we used the ECHAM6-wiso nudged simulation at T127L95 spatial resolution (0.9° horizontal resolution with 95 vertical hybrid sigma levels) from Cauquoin and Werner (2021). The 3D-fields of temperature, vorticity, and divergence, as well as the surface pressure field were nudged toward ERA5 reanalysis data (ref of ERA5). Isotopic boundary conditions were provided by the global dataset of LeGrande and Schmidt (2006), while sea surface temperature and sea-ice boundaries were also taken from ERA5. We used the 6-hourly outputs for the observational period i.e., 2020-2021. ECHAM6-wiso separately outputs specific humidity for two waters ("isotopic heavy water" and "normal light water"), and isotopic ratios were then represented to the "δ" notation in unit of per mil (‰). Gridded simulation data were interpolated onto the four monitoring stations based on their longitudes and latitudes and then averaged to daily and monthly time series. It should be noted that simulated isotope values in near-surface water vapor correspond to the first atmospheric layer above the land surface, which is approximately 60 m thick. Difference between the model's lowest atmospheric layer and the instrument inlet height may introduces bias in comparisons.

2.3 Ensemble Empirical Mode Decomposition (EEMD)

To decompose the non-linear and non-stationary time series of $\delta^{18}O_v$ into physically meaningful components, we applied Ensemble Empirical Mode Decomposition (EEMD), an advanced version of the Empirical Mode Decomposition (EMD) technique (Wu et al., 2009). EEMD mitigates the issue of mode mixing by adding white noise as the possible random noise that would be encountered in each "artificial" measurement to original signal and averaging the decomposition results over multiple realizations. The perturbed signal,

https://doi.org/10.5194/egusphere-2026-2351
Preprint. Discussion started: 20 May 2026

$$x_i(t) = x(t) + n_i(t) \quad (2)$$

where $x(t)$ is the original data series and $n_i(t)$ is the white noise added to the i-th realization. For each noisy version $x_i(t)$, EMD is performed as follows: (1) Identify all local maxima and minima; (2) Connect the extrema with cubic splines to form upper and lower envelopes; (3) Compute the mean envelope and subtract it from $x_i(t)$ to obtain a component; (4) Repeat process iteratively until the resulting component is nearly monotonic. After *n* realizations with different white noise, the ensemble average of each intrinsic mode function (IMF) is calculated to produce the final decomposition.

2.4 Improvement Potential Metric

To quantify the contribution of different temporal components to isotopic simulation errors, we define a metric called "improvement potential", based on EEMD decomposition results. The procedure is as follows: (1) Compute the root mean square error (RMSE) between the observed and original simulated daily $\delta^{18}O_v$ time series as $RMSE_{ori}$; (2) Apply EEMD to both observed and simulated time series, decomposing each into IMFs; (3) For each IMF, substitute the simulated component with the corresponding observed one and reconstruct the full signal; (4) Calculate RMSE of this modified simulated series relative to the observation, called $RMSE_{sub}$; (5) Define the improvement potential (IP), which is the relative deviation of the $RMSE_{sub}$ to $RMSE_{ori}$; (6) Repeat steps 3-5 for each IMF at each station, separately for monsoon and non-monsoon periods.

This metric identifies which temporal scales of time series contribute most to simulation discrepancies, and highlights where targeted model improvements may yield the greatest benefit.

3 Results

3.1 Comparisons of Atmospheric Variables

For spatial patterns, results from HARv2 show an obvious heterogeneity over the TP (Supplementary Fig. 3). In general, the eastern region of TP is warmer and more humid than the western. ECHAM6-wiso well simulates the general spatial patterns of 2 m air temperature and specific humidity over the TP. Particularly, the model captures detailed

https://doi.org/10.5194/egusphere-2026-2351
Preprint. Discussion started: 20 May 2026

spatial features. On the Chi-lien Mountains and Qaidam Basin, terrain-induced temperature heterogeneity is significant. The model reproduces fairly well this regional pattern, demonstrating a capability to perform reasonable simulation under complex TP topography.

Seasonal patterns in observed 2 m specific humidity, air temperature and precipitation amount are well simulated by ECHAM6-wiso for the four stations with an increase from January to July or August and a decline in the remaining months, showing consistent seasonal variations (Fig. 1). Higher values in those atmospheric variables are generally observed and modeled for the stations located on the southern TP (i.e., Kathmandu and Lulang). Besides precipitation, ECHAM6-wiso demonstrates the rather high correlations for the four stations with slightly overestimation or underestimation. For 2 m air temperature, the correlation coefficients are 0.85, 0.90, 0.88, and 0.91 at Kathmandu, Lulang, Namco and Muztag sites. For 2 m specific humidity, the correlation coefficients are 0.77, 0.86, 0.87, and 0.68. At Kathmandu site, ECHAM6-wiso slightly overestimates 2 m air temperature (13.06 ℃ in observation, while 14.88 ℃ in ECHAM6-wiso, annual averaged) and underestimates specific humidity (9.8 and 8.7 g/kg in observation and ECHAM6-wiso, respectively), obviously from January to April, which difference increases to -2.0 g/kg in average. At Lulang site, both simulated 2 m air temperature and specific humidity have been slightly overestimated (+1.58 ℃ and +1.44 g/kg). At Namco and Muztag sites, ECHAM6-wiso shows a quite well agreement with observed 2 m air temperature, but slightly overestimates specific humidity during the monsoon period (+0.88 g/kg and +0.48 g/kg).

Precipitation is the most challenging to model. At Kathmandu site, ECHAM6-wiso simulates generally too low precipitation amount, especially during the monsoon period. Averaged precipitation amount in observation is 12.67 mm/d at this site, while in ECHAM6-wiso is 10.95 mm/d. However, the model overestimates precipitation amount in the three other sites. Averaged monsoon precipitation amounts in observations are 10.24, 3.73, 1.19 mm/d at Lulang, Namco, and Muztag sites, while in ECHAM6-wiso are 15.26, 6.62, and 1.26 mm/d, respectively.

https://doi.org/10.5194/egusphere-2026-2351
Preprint. Discussion started: 20 May 2026

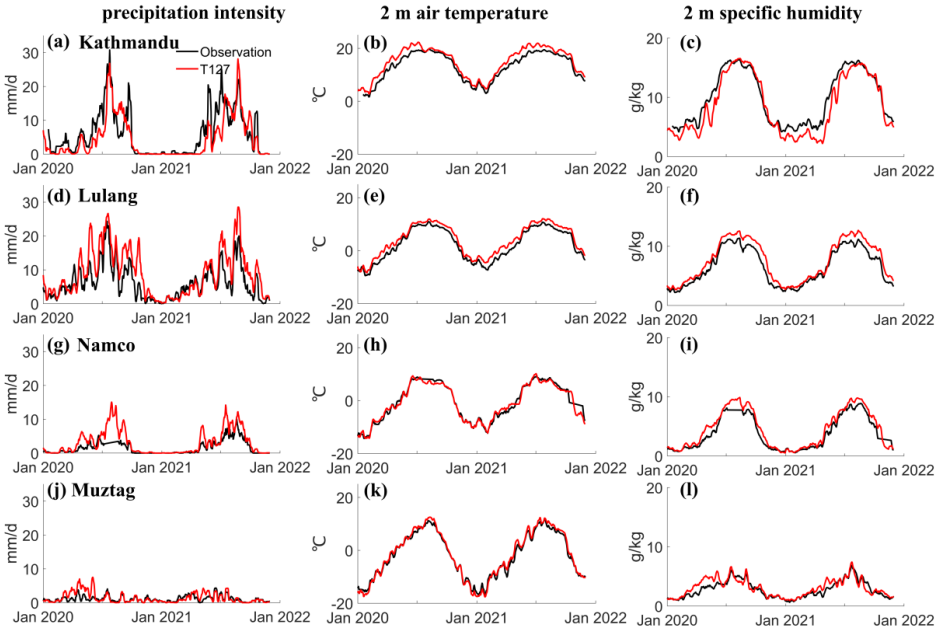

Figure 1. Daily time series of (a), (d), (g), (j) precipitation intensity [mm/d], (b), (e), (h), (k) 2 m air temperature [℃], and (c), (f), (i), (l) 2 m specific humidity [g/kg] at four monitoring stations. Red lines represent ECHAM6-wiso simulated results. Black lines indicate the observational values.

3.2 Spatiotemporal Patterns of Monthly Near-Surface $\delta^{18}O_v$

The $\delta^{18}O$ in near-surface water vapor ($\delta^{18}O_v$) over the TP exhibits two principal spatial patterns modulated by large-scale atmospheric circulation, as evidenced by monthly observational data (Fig. 2). These patterns correspond primarily to the seasonal dominance of the mid-latitude westerlies and the Indian summer monsoon. The monsoon period, extending from June to September, is characterized by moist air masses transported via southwestern and southeastern pathways. The remaining months comprise the non-monsoon period, during which the mid-latitude westerlies dominate. During the non-monsoon period, observed monthly $\delta^{18}O_v$ values display a clear meridional gradient (the "latitude effect"), with progressive isotopic depletion as the air masses move poleward (hereafter: meridional pattern). Kathmandu, the southernmost

https://doi.org/10.5194/egusphere-2026-2351
Preprint. Discussion started: 20 May 2026

monitoring station, shows the most enriched $\delta^{18}O_v$ values (-11.79‰, averaged of the non-monsoon period), while the northernmost station, Muztag, exhibits the most depleted values (mean: -30.71‰). Lulang and Namco exhibit intermediate $\delta^{18}O_v$ values (-19.93‰ and -23.72‰, respectively), consistent with their respective latitudinal positions. During the monsoon period, the meridional pattern transitions to a zonal (east-west) gradient. $\delta^{18}O_v$ values at Muztag increase markedly from -30.71‰ to -16.48‰ averagely, contrasting with persistently depleted conditions at Lulang and Namco site. This zonal isotopic distribution aligns with previous precipitation isotope studies (Yao et al., 2013).

Compared with the observations, ECHAM6-wiso effectively captures these different seasonal spatial patterns with enhanced spatial details. ECHAM6-wiso replicates latitudinal depletion during the non-monsoon period, including maximal isotopic enrichment south of the Himalayas (-12.38‰ in average), and the pre-monsoon shift of enriched $\delta^{18}O_v$ that initially expanding from the southeast TP and subsequently shifting toward the southwest (Supplementary Fig. 4b-e). The seasonal evolution is also well reproduced: as the monsoon weakens in September, it is clearly notice that the enriched $\delta^{18}O_v$ core starts retreat, flanked by more depleted air masses to the north and south (Supplementary Fig. 4j). In addition, corroborated by vertically integrated water vapor flux, relating a strong correspondence between moisture convergence zones and early-onset isotopic depletion. At the southeastern TP, the most isotopic depleted regions (from -18.31‰ in June to -24.57‰ in September) firstly occur and extend where moisture convergences are obvious as Indian summer monsoon continually develops (Supplementary Fig. 4f-h).

Time series analyses confirm that the observed seasonal cycles of monthly $\delta^{18}O_v$ are generally consistent, yet not perfectly synchronized with the monsoon and non-monsoon transition (Fig. 3). At Kathmandu and Lulang sites, $\delta^{18}O_v$ increases from September to April and decreases thereafter. For monitoring station closer to interior, Namco exhibits a similar seasonal cycle as at Kathmandu and Lulang but with weaker amplitude and higher variability. Muztag, in contrast, displays a distinct pattern: $\delta^{18}O_v$ rises from January to August and declines thereafter, with the largest amplitude among

https://doi.org/10.5194/egusphere-2026-2351
Preprint. Discussion started: 20 May 2026

all stations (from -39.29‰ in January to -14.26‰ in August).

ECHAM6-wiso simulation accurately replicates these seasonal cycles and amplitudes with fair fidelity at Kathmandu and Lulang sites. Quantitative evaluation shows that ECHAM6-wiso well simulates water vapor isotope ratios at seasonal-scale over the TP (Fig. 3e). A correlation coefficient greater than 0.6 ($p < 0.001$) is found for the four stations, accompanied by reasonable error margins. Model accuracy is particularly strong in the southern regions of the TP but decreases gradually with latitude, with greater bias at Muztag.

At Kathmandu site (Fig. 3a), the simulated increase in $\delta^{18}O_v$ during the non-monsoon period is weaker than the observations. At Lulang and Namco sites, simulations show persistent over-enrichment (Fig. 3b and c), which is even more severe at Namco site. Given that Namco site is located by the lake, reasons are likely due to deficiencies in representing lake-related fractionation processes (e.g., evaporation and condensation over lake surface). At Muztag site (Fig. 3d), the simulated seasonal amplitude is too small and peaks two months too early. Errors are especially pronounced during the non-monsoon period.

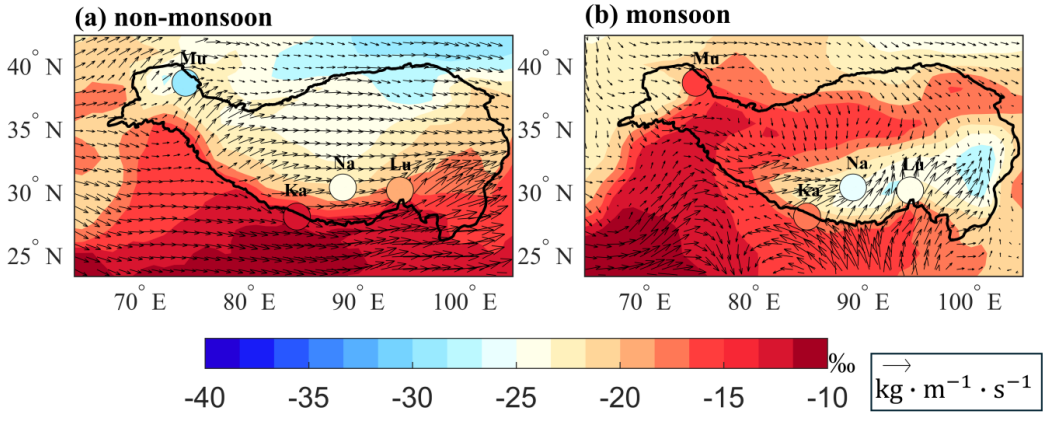

Figure 2. Distributions of simulated (colored contours) and observed (colored dots) monthly mean near-surface $\delta^{18}O_v$ values [‰] during (a) non-monsoon and (b) monsoon periods, averaged of period 2020-2021. Black arrows denote the simulated vertically integrated water vapor flux [$kg \cdot m^{-1} \cdot s^{-1}$], while the black polygon outlines

https://doi.org/10.5194/egusphere-2026-2351
Preprint. Discussion started: 20 May 2026

the TP border. Four monitoring stations are informed by abbreviation: Kathmandu (Ka), Lulang (Lu), Namco (Na), and Muztag (Mu).

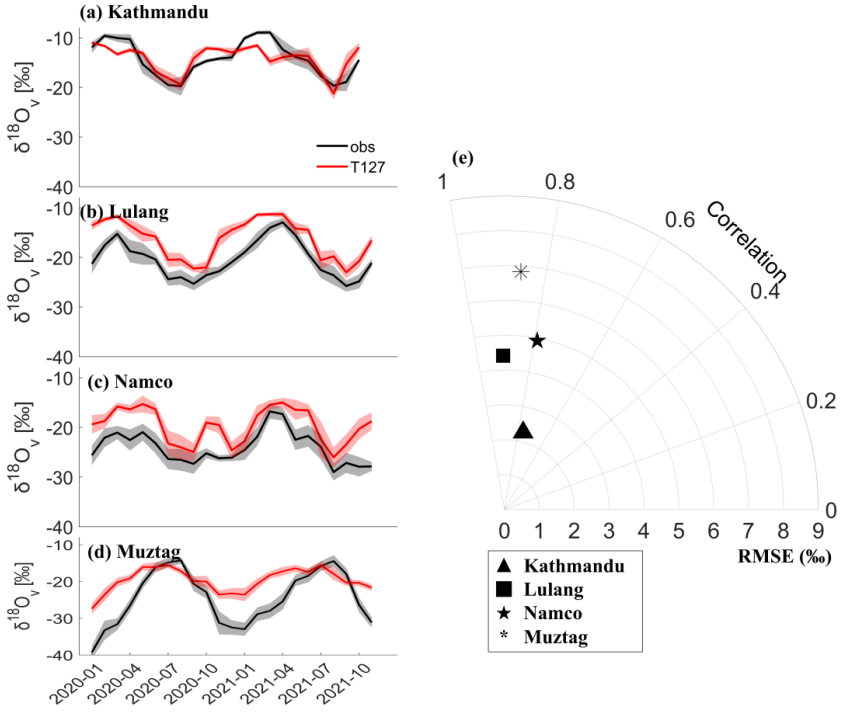

Figure 3. Monthly time series of near-surface $\delta^{18}O_v$ at (a) Kathmandu, (b) Lulang, (c) Namco, and (d) Muztag. (e) Projection of correlation coefficients and RMSEs for monthly $\delta^{18}O_v$ time series. The red lines represent the ECHAM6-wiso simulated results, while observations are shown as black lines. The envelopes indicate monthly variability. In panel (e), a higher radial value indicates higher error; angle indicates correlation (close to left=better). Stations markers: Kathmandu (upward triangle), Lulang (square), Namco (pentagram), and Muztag (asterisk).

3.3 Different Phase Seasonal Cycle of $\delta^{18}O_v$ at Muztag

The distinct seasonal behavior of $\delta^{18}O_v$ observed at Muztag deviates markedly from the other sites, suggesting fundamentally different mechanisms controlling isotopic variation. Given that $\delta^{18}O_v$ variation is defined by changes in the ratio of "isotopic

https://doi.org/10.5194/egusphere-2026-2351
Preprint. Discussion started: 20 May 2026

heavy water" to "normal light water", its variability reflects not only the abundance of humidity but also fractionation processes. In addition, when multiple processes operate simultaneously (some reinforcing and others offsetting), it is challenging to disentangle the driving factors behind $\delta^{18}O_v$ anomalies.

An advantage of isotope-enabled AGCMs like ECHAM6-wiso is their ability to separately simulate the transport of "normal light water" ($H_2{}^{16}O$) and "heavy isotopic water" ($HD^{16}O$ and $H_2{}^{18}O$), facilitating detailed diagnostic analyses of isotopic variations. Simulated "normal light water" at the southern monitoring stations (Kathmandu, Lulang, and Namco) shows a gradual increase from January to July/August, followed by sharp decline after September (from 1.29 g/kg to 8.88 g/kg in average). At Muztag site, while "normal light water" also rises until July, its amplitude is less pronounced (Fig. 4a). Simulated "heavy isotopic water" shows an almost same change as "normal light water" but with a much lower magnitude.

Importantly, by decoupling change of two waters, the seasonal $\delta^{18}O_v$ pattern stems not from divergent trends in two water mass concentrations, but from a mismatch in the rates of change between "normal light water" and "isotopic heavy water". Thus, to quantify this mismatch, we define a metric termed the "multiple factor", the ratio of change of "isotopic heavy water" to that of "normal light water" ($f = \frac{q_{iso,t+1}/q_{iso,t}}{q_{t+1}/q_t}$, Fig. 4b). A value of $f < 1$ implies that "isotopic heavy water" increases more slowly or decreases more rapidly than "normal light water", signaling intensified isotopic fractionation (e.g., more precipitation en route) happened during atmospheric transport or a shift in water vapor source region toward more isotopically depleted regions. Conversely, a value of $f > 1$ suggests that faster increase or slower decrease in "isotopic heavy water" than "normal light water", indicating that the water vapor source is either becoming isotopically enriched or shifting toward more enriched regions.

At Kathmandu, Lulang, and Namco, $f > 1$ between September and March, peaking in the immediate post-monsoon period (September to November), before dropping below 1 during the core monsoon months (June-September). This is consistent with enhanced fractionation along longer atmospheric transport paths during the monsoon onset and

https://doi.org/10.5194/egusphere-2026-2351
Preprint. Discussion started: 20 May 2026

decay. In contrast, Muztag exhibits a nearly opposite phase pattern: f > 1 from January through July and drops below 1 thereafter. This unique pattern in the relative dynamics of "normal light water" and "isotopic heavy water" consequently yield its distinct seasonal $\delta^{18}O_v$ cycle. Compared to other sites, the multiple factor and water mass concentration at Muztag site show in-phase change, suggests they may be modulated by same mechanisms (e.g., meridional oscillation of atmospheric transport).

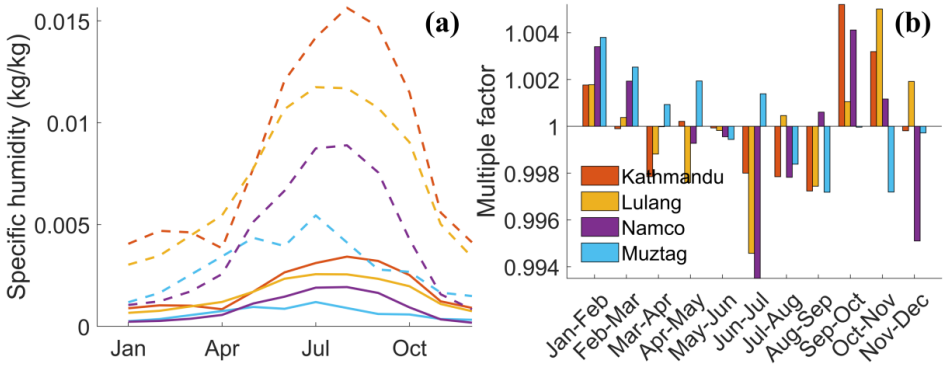

Figure 4. (a) Monthly time series of simulated specific humidity [kg/kg] for "normal light water" ($H_2^{16}O$; dashed lines) and "isotopic heavy water" ($H_2^{18}O$; solid lines) at four stations, averaged over 2020-2021. (b) Monthly evolution of the multiple factors, defined as the ratio of the monthly rate of change in $H_2^{18}O$ to that of $H_2^{16}O$. Colors represent Kathmandu (orange), Lulang (yellow), Namco (purple), and Muztag (light blue).

3.4 Deficiencies of Simulated Daily $\delta^{18}O_v$

Differences between simulated and observed daily $\delta^{18}O_v$ values show a general overestimation in ECHAM6-wiso, especially during the non-monsoon period (Fig. 5a). Scatter plots comparing daily observed and simulated $\delta^{18}O_v$ reinforce these findings (Fig. 5b). Across all sites, the simulation exhibits a systematic positive bias, particularly for low $\delta^{18}O_v$ values (i.e., underestimating isotopic depletion). Observations range from -45.80‰ to -6.57‰, but the model fails to reproduce both tails of the distribution. Specifically, at Kathmandu, ECHAM6-wiso obviously underestimates the most

https://doi.org/10.5194/egusphere-2026-2351
Preprint. Discussion started: 20 May 2026

enriched $\delta^{18}O_v$ values, misclassifying values in [-12‰, -6‰] as falling in [-20‰, -12‰]. At Lulang and Namco, simulated daily $\delta^{18}O_v$ values consistently show positive deviations across the full range of observations, reflecting overestimated vapor enrichment. At Muztag, observed $\delta^{18}O_v$ values below -27‰ are systematically overestimated by the model, indicating a failure of model to depict mechanisms that deplete $\delta^{18}O_v$ values.

While ECHAM6-wiso captures the seasonal-scale behavior of $\delta^{18}O_v$ over the TP with reasonable accuracy (Fig. 3e), its performance degrades significantly when evaluated against daily observational records (Fig. 5c). Although correlation coefficients remain positive ($r > 0.6$, $p < 0.001$) at four sites, they are notably lower than those for the monthly data. This reflects the model's limited skill in resolving short-term variability in $\delta^{18}O_v$, particularly at higher latitudes and more inland locations such as Muztag site. A comparison of probability-density functions (PDFs) for observed and simulated daily $\delta^{18}O_v$ values further illustrate the model deficiencies (Fig. 6). Observed PDFs exhibit the spatial heterogeneity consistent with the "latitude effect", with increasingly depleted modes moving northward, except at Muztag, where a bimodal distribution emerges, suggesting durations of different mechanisms affecting $\delta^{18}O_v$ are relatively consistent (Supplementary Fig. 5).

Despite capturing the overall shape of the observed PDFs, ECHAM6-wiso consistently overestimates $\delta^{18}O_v$ values, and misrepresents the tails of the distributions: 1) At Kathmandu, observed values are mainly concentrated in range [-20‰, -8‰] (density ≥ 0.1), yet ECHAM6-wiso fails to reproduce the most enriched extremes, instead shifting probability toward more depleted values, especially in the range [-14‰, -10‰] (Fig. 6a); 2) At Lulang and Namco, observed probabilities peak between [-26‰, -16‰] and [-28‰, -18‰], respectively, but the model shifts the distributions significantly higher $\delta^{18}O_v$, with peak densities [-18‰, -10‰] and [-20‰, -14‰], respectively (Fig. 6b and c); 3) At Muztag, the observed bimodal structure (peaks near -29‰ and -15‰) is not captured by ECHAM6-wiso, which instead produces a unimodal distribution centers near [-22‰, -14‰] (Fig. 6d). This indicates that ECHAM6-wiso may fails to precisely reproduce the transition between mechanisms that affect $\delta^{18}O_v$ values.

https://doi.org/10.5194/egusphere-2026-2351
Preprint. Discussion started: 20 May 2026

Moreover, it is important to account for the vertical mismatch between modelled and observed values. Simulated near-surface $\delta^{18}O_v$ corresponds to the lowest atmospheric model level (~60 m above ground surface), whereas observations were made closer to the surface (~2-5 m). If simulated values are linearly extrapolated to the observational height, given that profile of simulated $\delta^{18}O_v$, actual overestimation might be even more obvious.

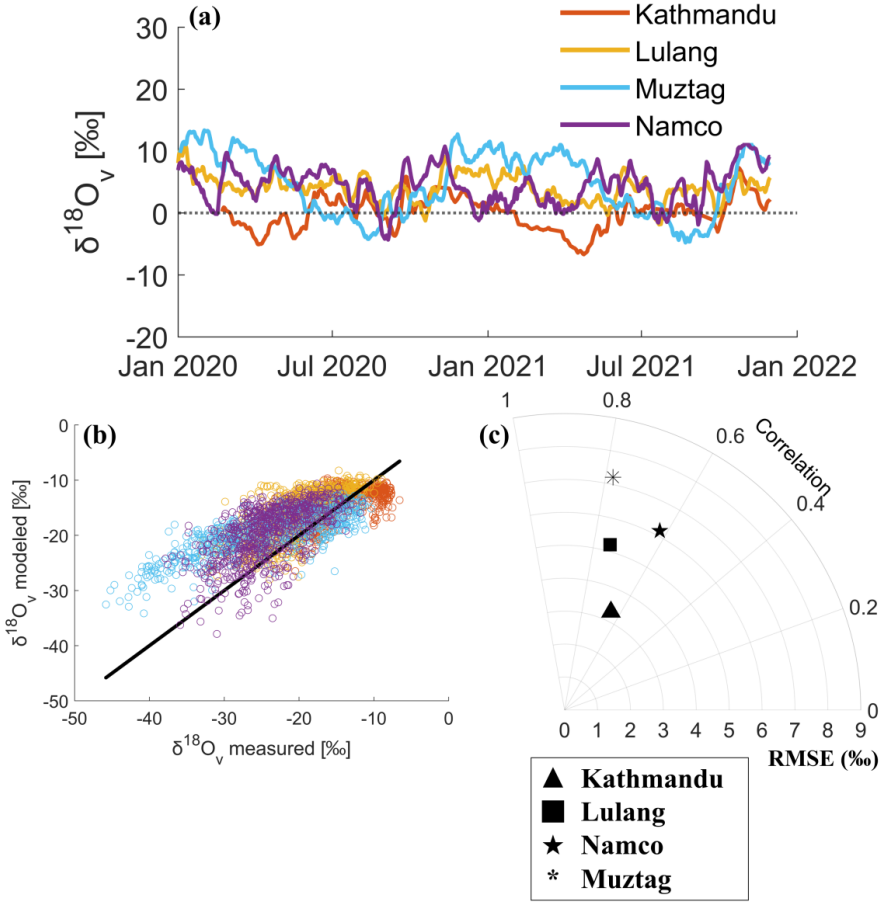

Figure 5. (a) Daily time series of simulated $\delta^{18}O_v$ values minus observed. (b) Scatter plots comparing observed and simulated daily $\delta^{18}O_v$. (c) Projection of correlation coefficients and RMSEs for daily $\delta^{18}O_v$ time series. In panels (a) and (b), colors indicate stations: Kathmandu (orange), Lulang (yellow), Namco (purple), and Muztag (light blue). In panel (b), black line indicates the values the model would have

https://doi.org/10.5194/egusphere-2026-2351
Preprint. Discussion started: 20 May 2026

493 if it exactly matched observations. In panel (c), a higher radial value indicates higher
494 error; angle indicates correlation (close to left=better). Stations markers: Kathmandu
495 (upward triangle), Lulang (square), Namco (pentagram), and Muztag (asterisk).
496

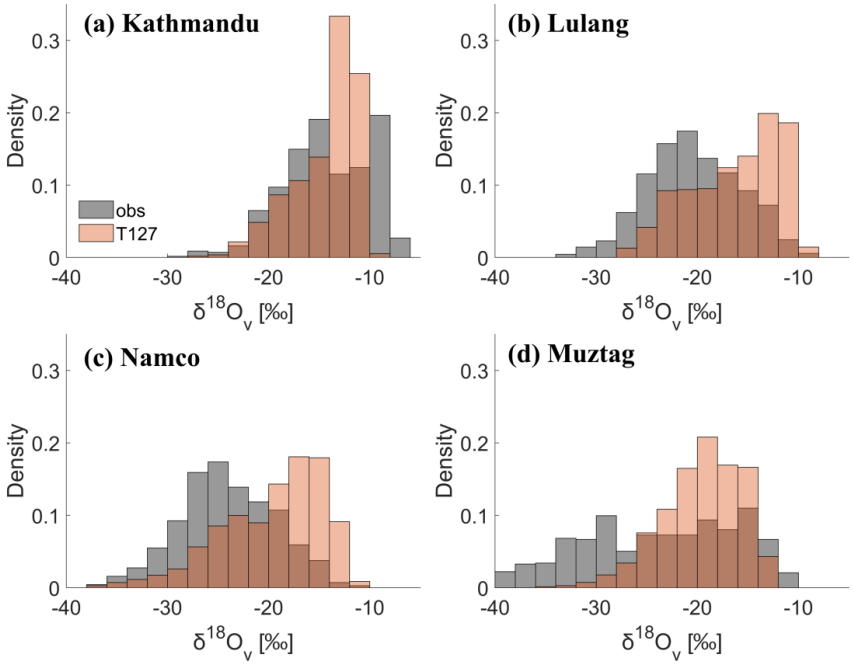

497

498 **Figure 6. Probability density functions (PDFs) of observed and simulated daily**
499 **near-surface $\delta^{18}O_v$ at: (a) Kathmandu, (b) Lulang, (c) Namco, and (d) Muztag.**
500 Gray bars: observations; orange bars: ECHAM6-wiso simulation.
501

502 **3.5 Error Attribution of Simulated Daily $\delta^{18}O_v$**

503 We begin the attribution analyses by examining conventional drivers of $\delta^{18}O_v$ variability,
504 temperature and precipitation, which influence fractionation through thermodynamic
505 and removal processes, respectively. Theoretically, warmer air mass would reduce
506 equilibrium fractionation (i.e., resulting in less $\delta^{18}O_v$ depletion), while increased
507 precipitation intensity typically enhances isotopic depletion via the "amount effect"
508 (Galewsky et al., 2016). When ignoring other control factors, if a model simulates a

https://doi.org/10.5194/egusphere-2026-2351
Preprint. Discussion started: 20 May 2026

warm bias in temperature or dry bias in precipitation intensity, simulated $\delta^{18}O_v$ values would present a positive bias, the reverse is true. However, ECHAM6-wiso exhibits inconsistent relationships between these two drivers and $\delta^{18}O_v$ biases, suggesting that these first-order controls do not fully explain the model deficiencies.

At Kathmandu site, the model exhibits a warm bias from January to May (Fig.1b), which would typically reduce $\delta^{18}O_v$ fractionation. Yet, the modeled $\delta^{18}O_v$ shows a negative deviation (Fig. 5a), which is opposite of to what is expected. At Lulang site, during the monsoon period, the model simulates a moist bias (Fig. 1d), which should produce more depleted $\delta^{18}O_v$, but instead the model overestimates $\delta^{18}O_v$ (Fig. 5a). At Namco site, simulated precipitation intensity exhibits a strong moist bias during the monsoon period (Fig. 1g), yet the model still overestimates $\delta^{18}O_v$, again inconsistent with expectations. At Muztag site, simulated biases in temperature and precipitation cannot reflect significant underestimation of isotopic depletion during the non-monsoon period. These findings confirm that classical explanatory variables (temperature and precipitation) do not adequately capture the origins of model bias in $\delta^{18}O_v$. The progressively removal processes during atmospheric transport, even atmospheric circulation itself, might also has significant impact on isotopic simulation error.

However, it is hard to examine relationship between atmospheric circulation and simulated $\delta^{18}O_v$ biases by selecting exact variable. On the other hand, variation of $\delta^{18}O_v$ is influenced by multiple processes operating at distinct time scales, resulting in daily $\delta^{18}O_v$ time series composed of rapid fluctuations superimposed on signals with longer periodicities. Therefore, decomposing such complex time series into distinct periodic components significantly facilitates error attribution analyses.

We employed Ensemble Empirical Mode Decomposition (EEMD) to isolate the dominant temporal components in the simulated and observed daily $\delta^{18}O_v$ series (see Methods). We extracted five primary components, representing distinct temporal scales: sub-weekly (2-3 days), weekly (3-7 days), biweekly (7-15 days), monthly (15-45 days), and seasonal (45-90+ days). These decomposed components were then used to assess error attributions and identify the dominant time scales responsible for model bias in

https://doi.org/10.5194/egusphere-2026-2351
Preprint. Discussion started: 20 May 2026

both monsoon and non-monsoon periods (Fig. 7).

During the non-monsoon period, errors at seasonal scale dominate across all sites, contributing over 50% of the total RMSE (Fig. 7a). As variations above monthly scale are mainly modulated by atmospheric circulations, this suggests that a bias in large-scale atmospheric circulation patterns in ECHAM6-wiso.

During the monsoon period, the error structures are more variable (Fig. 7b). A higher contribution from shorter time scales (e.g., sub-weekly and weekly) is only found at Kathmandu site, situated on the southern slope of the Himalayas, whereas longer time scales (e.g., monthly and seasonal) contribute less than 50% (44.15%). The increased error contribution from shorter time scales implies the more frequency or error in synoptic-scale events during atmospheric transport. Error structures similar to the ones in non-monsoon period are found in Lulang and Namco sites, with dominant contributions from low frequency (monthly and seasonal) components (57.12% and 61.09%, respectively). These different error structures on south and north sides of the Himalayas imply a pronounced impact of the Himalayan topography on simulation of atmospheric circulation. As atmospheric moisture transporting across the Himalayas, circulation-related error (longer time scales) gradually greater than convective-related (shorter time scales) and become the primary origin of error. At Muztag site, located on the northwestern TP, contributions at various time scales are relatively balanced, suggesting equal importance of large-scale atmospheric circulations and frequent convective events.

To understand what happens when ECHAM6-wiso simulates atmospheric circulation over the TP, the TP border was demarcated into 13 transects referred to Liu et al. 2024 (see Supplementary materials for details), and evaluation of atmospheric moisture transport was conducted in each transect. The spatial patterns of atmospheric moisture transport around the TP and inflow profiles in transect 4 (near the Himalayas) for this study are shown in Figure 8.

Owing to the extreme elevation of the TP, which significantly exceeds the surrounding topography, regional moisture transport across the Himalayas is physically constrained above the 800 hPa level (Fig. 8a). However, ECHAM6-wiso erroneously simulates

https://doi.org/10.5194/egusphere-2026-2351
Preprint. Discussion started: 20 May 2026

significant land-terminating moisture flux below this pressure level (Fig. 8b). This failure to capture the topographic blocking effect leads to a pronounced simulation bias, wherein excessive moisture is artificially transported into the TP interior. Crucially, because this spurious moisture bypasses the physical barrier of the Himalayas in the model, it does not undergo the requisite topographic lifting and subsequent orographic rainout. Consequently, the simulated water vapor remains isotopically enriched due to the absence of Rayleigh-type distillation during ascent. This process results in a systematic overestimation of δD_v and $\delta^{18}O_v$ values across the Himalayas. Furthermore, rather than being redirected by the high terrain (Fig. 8c), the moisture is incorrectly routed directly onto the Plateau, fundamentally altering the modeled spatial patterns of transport (Fig. 8d). Given that ECHAM6-wiso is nudged toward ERA5, an analysis of the ERA5 inflow profiles (Supplementary Fig. 7) reveals similar non-physical moisture flux below 800 hPa. These results suggest that the misrepresentation of terrain-induced blocking may stem from the specific nudging implementation or the inherent limitations of the model's horizontal resolution in resolving steep alpine gradients.

We introduced the concept of "improvement potential", defined as a theoretical metric quantifying the residual model accuracy gain achievable if a specific temporal frequency were simulated with zero variance error. This metric mirrors the error contribution patterns, reaffirming the disproportionate contribution of low frequency components represents the primary bottleneck for model performance.

During the non-monsoon period, a selective correction of low-frequency scales (i.e., monthly and seasonal) reduces the total Root Mean Square Error (RMSE) by over 50% across all observation sites (Fig. 9a). This underscores that refining the simulation of large-scale atmospheric circulation, such as the positioning and intensity of the westerly jet, should be a prioritized objective for model development over the TP. Conversely, during the monsoon period, the relative importance of high-frequency variability increases at Kathmandu and Muztag sites. This shift is likely attributable to the increased frequency of synoptic-scale frontal systems or localized mesoscale convective disturbances (Fig. 9b). However, at Lulang and Namco sites, the low-frequency components remain the dominant drivers of model improvement. This

https://doi.org/10.5194/egusphere-2026-2351
Preprint. Discussion started: 20 May 2026

599 persistence suggests that terrain-induced systematic biases along the Himalayas are
600 exert a first-order control on isotopic variance, effectively overwhelming the stochastic
601 errors associated with transient synoptic processes.

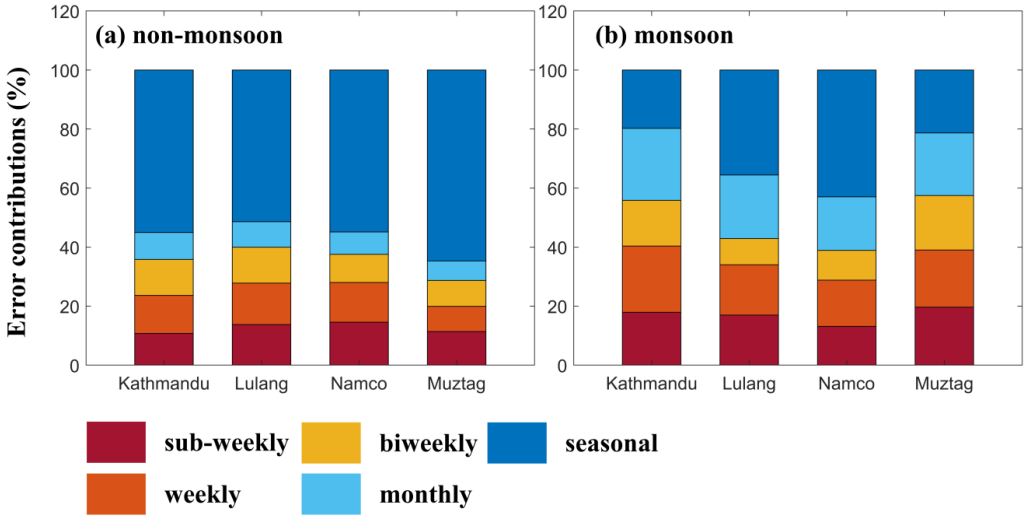

602

603 **Figure 7. Error contributions for $\delta^{18}O_v$ simulations across time scales during (a)**
604 **non-monsoon and (b) monsoon periods.** Time scales: sub-weekly (dark red), weekly
605 (orange), biweekly (yellow), monthly (light blue), and seasonal (blue).

606

https://doi.org/10.5194/egusphere-2026-2351
Preprint. Discussion started: 20 May 2026

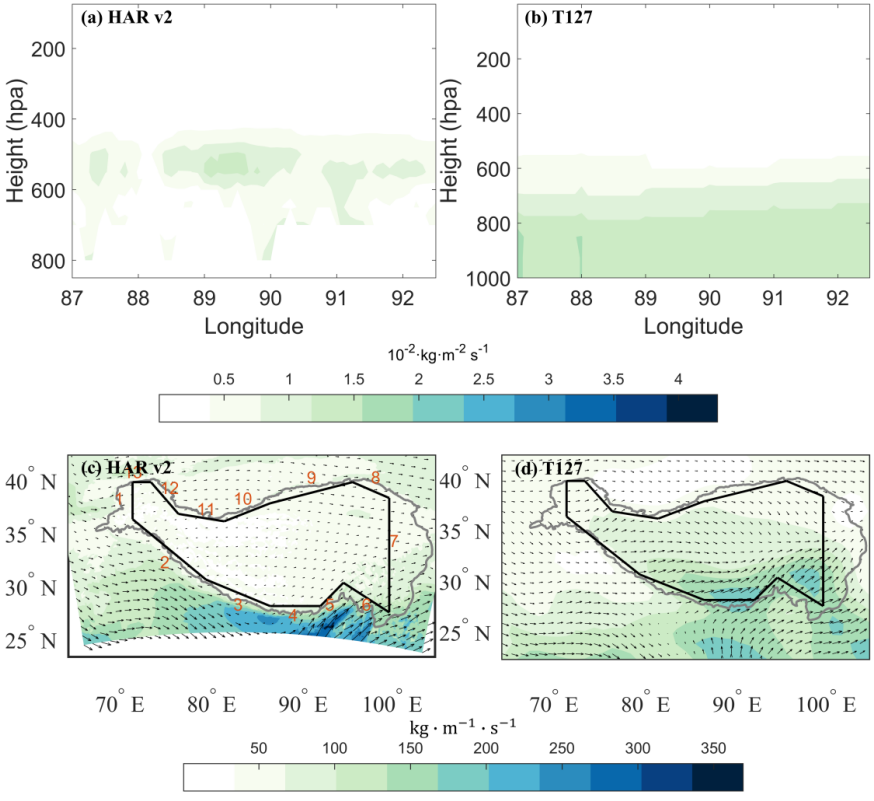

607

608 **Figure 8. (a), (b) Inflow profiles [10^{-2} kg m^{-2} s^{-1}] on transect 4. (c), (d) Atmospheric**
609 **moisture transport (vertically integrated water vapor flux) [kg m^{-1} s^{-1}].** In panel (a),
610 (b), inflow profiles are perpendicular vector values of atmospheric moisture transport
611 relative to transect 4 at each pressure level. In panel (c), (d), black arrows denote the
612 vertically integrated water vapor flux, while the gray polygon outlines the TP border.
613 The black lines show location of the 13 transects.

614

https://doi.org/10.5194/egusphere-2026-2351
Preprint. Discussion started: 20 May 2026

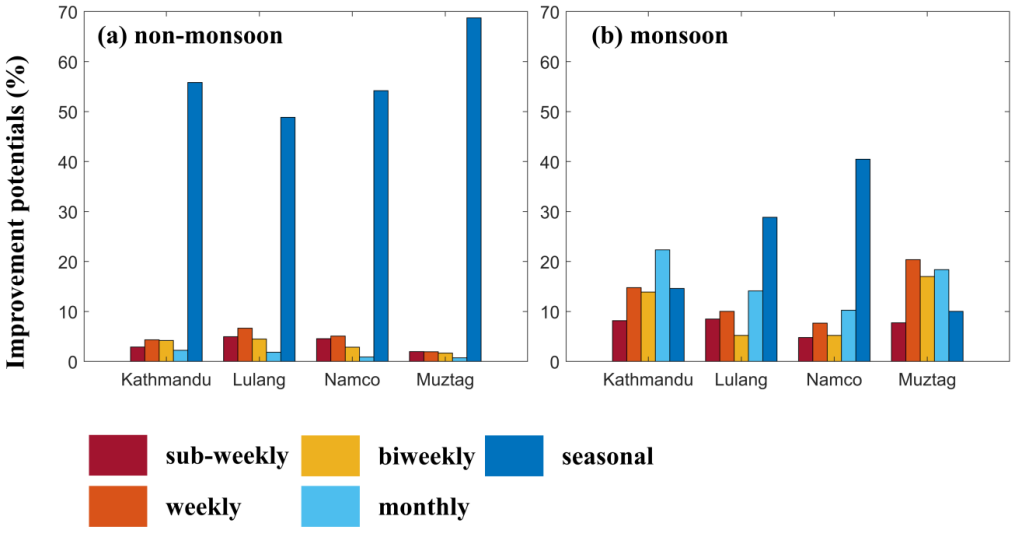

Figure 9. "Improvement potential" for $\delta^{18}O_v$ simulations across time scales during (a) non-monsoon and (b) monsoon periods. Time scales: sub-weekly (dark red), weekly (orange), biweekly (yellow), monthly (light blue), and seasonal (blue).

4 Conclusions

For several decades, evaluations of isotope-enabled atmospheric general circulation models (iAGCMs) over the TP have primarily relied on precipitation stable isotopes, due to the scarcity of high-resolution atmospheric water vapor isotopic measurements. This study addresses this gap by utilizing a unique daily observational dataset (January 2020−November 2021) from four strategically located high-altitude stations (Kathmandu, Lulang, Namco, and Muztag). We provide the first systematic evaluation of ECHAM6-wiso's ability to simulate water vapor stable isotope ratios ($\delta^{18}O_v$) in the near-surface atmosphere over the TP.

Our results demonstrate that while ECHAM6-wiso successfully captures the overarching spatial distribution and seasonal cycle of $\delta^{18}O_v$, its performance exhibits a distinct latitudinal gradient, with higher fidelity in the southern TP. Notably, the unique seasonal cycle observed at the Muztag site, driven by a kinetic mismatch in the rates of change between light and heavy isotopologues, is reproduced by ECHAM6-wiso, albeit

https://doi.org/10.5194/egusphere-2026-2351
Preprint. Discussion started: 20 May 2026

with persistent deficiencies. Despite these seasonal successes, model performance degrades significantly at the synoptic scale. We identify a systematic positive bias, specifically an underestimation of isotopic depletion during low $\delta^{18}O_v$ events, which points to fundamental errors in the simulation of moisture distillation processes.

To diagnose the drivers of these biases, we employed the Ensemble Empirical Mode Decomposition (EEMD) technique to isolate the dominant temporal components ranging from sub-weekly to seasonal scales in the simulated and observed daily $\delta^{18}O_v$ series. Our analysis reveals that low-frequency components (monthly and seasonal) dominate the simulation error across all sites, particularly during the non-monsoon period, where they contribute over 50% of the total Root Mean Square Error (RMSE). These errors are physically linked to the model's inability to resolve terrain-induced atmospheric moisture blocking along the Himalayan arc. By incorrectly transporting moisture directly onto the Plateau, a bias mirrored in the ERA5 nudging data, the model fundamentally distorts the spatial patterns of moisture flux. This suggests that the nudging implementation or insufficient horizontal resolution remains a primary bottleneck for isotopic accuracy in regions of steep topography.

We further introduced the "improvement potential" metric, which quantifies the theoretical accuracy gain achievable by resolving specific temporal scales. This indicator confirms that prioritizing the refinement of low-frequency, large-scale atmospheric circulation could reduce total RMSE by more than 50% during the non-monsoon period. Our findings align with previous global and regional studies (e.g., Steen-Larsen et al., 2016; Shi et al., 2022) which reported similar positive biases in iAGCMs over Greenland and the TP. However, this study advances the field by quantifying the contribution of these errors and identifying the topographic-circulation nexus as the primary source of isotopic distortion.

In summary, these results underscore the critical role of resolved atmospheric circulation in stable isotope simulations. Our findings highlight the necessity of high-resolution isotopic datasets to refine moisture source attribution and water-cycle dynamics in complex alpine environments.

https://doi.org/10.5194/egusphere-2026-2351
Preprint. Discussion started: 20 May 2026

Code and data Availability

The HARv2 data set can be obtained from: https://data.klima.tu-berlin.de/HAR/ (Wang et al., 2021). The observational data and model outputs at Kathmandu, Lulang, Muztag, and Namco are publicly available at: https://doi.org/10.6084/m9.figshare.31900747 (Liu et al., 2026a) and https://doi.org/10.6084/m9.figshare.31900705 (Liu et al., 2026b). Core representative analysis scripts used to evaluate model performance are openly available at: https://doi.org/10.6084/m9.figshare.31900777 (Liu et al., 2026c).

Acknowledgements

This work was funded by The Second Tibetan Plateau Scientific Expedition and Research (STEP) program (Grant No. 2024QZKK0400) and the Key Research and Development and Transformation Project of the Tibet Science and Technology Program (Grant no. XZ202501ZY0081). We acknowledge staffs at the four observational stations for providing support on water vapor isotopic observation.

Financial support

This work was funded by The Second Tibetan Plateau Scientific Expedition and Research (STEP) program (Grant No. 2024QZKK0400) and the Key Research and Development and Transformation Project of the Tibet Science and Technology Program (Grant no. XZ202501ZY0081).

Author contributions

Y.G.L.: Wrote original draft, Data processing, Visualization, Analysis. J.G.: Supervision, Reviewing, Editing, Analysis. M.W.: Reviewing, Editing, Analysis. A.C.: Reviewing, Editing, Analysis. K. L.: Data processing, Analysis.

Correspondence to Jing Gao (gaojing@itpcas.ac.cn)

Competing interests

The authors declare no competing interests.

https://doi.org/10.5194/egusphere-2026-2351
Preprint. Discussion started: 20 May 2026

References

Adhikari, N., Gao, J., Zhao, A., Xu, T., Chen, M., Niu, X., and Yao, T. (2024). Spring tropical cyclones modulate near-surface isotopic compositions of atmospheric water vapour in Kathmandu, Nepal. Atmos. Chem. Phys., 24, 3279-3296, https://doi.org/10.5194/acp-24-3279-2024.

Baer, D. S., Paul, J. B., Gupta, M., and O'Keefe, A. (2002). Sensitive absorption measurements in the near-infrared region using off-axis integrated cavity output spectroscopy. Appl. Phys. B, 75, 261–265, https://doi.org/10.1007/s00340-002-0971-z.

Cauquoin, A., Werner, M., and Lohmann, G. (2019). Water isotopes – climate relationships for the mid-Holocene and preindustrial period simulated with an isotope-enabled version of MPI-ESM. Clim. Past, **15**, 1913-1937, https://doi.org/10.5194/cp-15-1913-2019.

Cauquoin, A., and Werner, M. (2021). High-Resolution Nudged Isotope Modeling With ECHAM6-Wiso: Impacts of Updated Model Physics and ERA5 Reanalysis Data. J. Adv. Model. Earth Syst., **13**, e2021MS002532, https://doi.org/10.1029/2021MS002532.

Chen, M., Gao, J., Luo, L., Zhao, A., Niu, X., Yu, W., Liu, Y., and Chen, G. (2024). Temporal variations of stable isotopic compositions in atmospheric water vapor on the Southeastern Tibetan Plateau and their controlling factors. Atmospheric Research, **303**, 107328, https://doi.org/10.1016/j.atmosres.2024.107328.

Ciais, P., and Jouzel, J. (1994). Deuterium and Oxygen 18 in Precipitation: Isotopic model, including mixed could processes. J. Geophys. Res., **99**, 16793-16803, https://doi.org/10.1029/94JD00412.

Craig, H. (1961). Isotopic variations in meteoric waters. Science, **133**, 1702–1703, https://doi.org/10.1126/science.133.3465.1702.

Crosson, E. R., Ricci, K. N., Richman, B. A., Chilese, F. C., Owano, T. G., Provencal, R. A., Todd, M. W., Glasser, J., Kachanov, A. A., Paldus, B. A., Spence, T. G., and Zare, R. N. (2002). Stable isotope ratios using cavity ring-down spectroscopy: Determination of $^{13}C/^{12}$ for carbon dioxide in human breath. Anal. Chem., **74**,

https://doi.org/10.5194/egusphere-2026-2351
Preprint. Discussion started: 20 May 2026

2003–2007, https://doi.org/10.1021/ac025511d.

Dansgaard, W. (1954). The O^{18}-abundance in fresh water. Geochimica et Cosmochimica Acta, **6**, 241–260, https://doi.org/10.1016/0016-7037(54)90003-4.

Dansgaard, W. (1964). Stable isotopes in precipitation. Tellus, **16**, 436-468, https://doi.org/10.1111/j.2153-3490.1964.tb00181.x.

Epstein, S., and Mayeda, T. (1953). Variation of O^{18} content of waters from natural sources. Geochimica et Cosmochimica Acta, **4**, 213–224, https://doi.org/10.1016/0016-7037(53)90051-9.

Finkenbiner, C. E., Li, B., Spencer, L., Butler, Z., Haagsma, M., Fiorella, R. P., Allen, S. T., Anderegg, W., Still, C. J., Noone, D., Bowen, G. J., and Good, S. P. (2022). The NEON Daily Isotopic Composition of Environmental Exchanges Dataset. Sci. Data, **9**, 353, https://doi.org/10.1038/s41597-022-01412-4.

Galewsky, j., Steen-Larsen, H. C., Field, R. D., Worden, J., Risi, C., and Schneider, M. (2016). Stable isotopes in atmospheric water vapor and applications to the hydrologic cycle. Reviews of Geophysics, **54**, 809–865, https://doi.org/10.1002/2015RG000512.

Gao, J., Masson-Delmotte, V., Yao, T., Tian, L., Risi, C., Hoffmann, G. (2011). Precipitation water stable isotopes in the south Tibetan Plateau: observation and modeling. J. Climate, **24**, 3161-3178, https://doi.org/10.1175/2010JCLI3736.1.

Gao, J., Masson-Delmotte, V., Risi, C., He, Y., and Yao, T. (2013). What controls precipitation $\delta^{18}O$ in the southern Tibetan plateau at seasonal and intra-seasonal scales? A case study at Lhasa and Nyalam. Tellus B: Chemical and Physical Meteorology, **65**, 21043, https://doi.org/10.3402/ tellusb.v65i0.21043.

Gao, J., Yao, T., Masson-Delmotte, V., Steen-Larsen, H. C., and Wang, W. (2019). Collapsing glaciers threaten Asia's water supplies. Nature, **565**, 19-21, https://doi.org/10.1038/d41586-018-07838-4.

Gat, J. R. (1996). Oxygen and hydrogen isotopes in the hydrological cycle. Annual Review of Earth and Planetary Sciences, **24**, 225–262, https://doi.org/10.1146/annurev.earth.24.1.225.

Haese, B., Werner, M., and Lohmann, G. (2013). Stable water isotopes in the coupled

https://doi.org/10.5194/egusphere-2026-2351
Preprint. Discussion started: 20 May 2026

atmosphere-land surface model ECHAM5-JSBACH. Geosci. Model Dev., **6**, 1463-1480, https://doi.org/10.5194/gmd-6-1463-2013.

He, Y., Risi, C., Gao, J., Masson-Delmotte, V., Yao, T., Lai, C., Ding, Y., Worden, J., Frankenberg, C., Chepfer, H., and Cesana, G. (2015). Impact of atmospheric convection on south Tibet summer precipitation isotopologue composition using a combination of in situ measurements, satellite data, and atmospheric general circulation modeling. Journal of Geophysical Research: Atmospheres, **120**, 3852-3871, https://doi.org/10.1002/2014jd022180.

Hoffmann, G., Werner, M., and Heimann, M. (1998). Water isotope module of the ECHAM atmospheric general circulation model: A study on timescales from day to several years. J. Geophys. Res., **103**, 16871-16896, https://doi.org/10.1029/98JD00423.

Horibe, Y., and Ogura, N. (1968). Deuterium content as a parameter of water mass in the ocean. J. Geophys. Res., **73**, 1239-1249, https://doi.org/10.1029/JB073i004p01239.

Immerzeel, W. W., Van Beek, L. P. H., and Bierkens, M. F. P. (2010). Climate change will affect the Asian water towers. Science, **328**, 1382–1385, https://doi:10.1126/science.1183188.

Joussaume, S., Sadourny, R., and Jouzel, J. (1984). A general circulation model of water isotope cycles in the atmosphere. Nature, **331**, 24-29, https://doi.org/10.1038/311024a0.

Jouzel, J., and Merlivat, L. (1984). Deuterium and Oxygen 18 in Precipitation: Modeling of the Isotopic Effects During Snow Formation. J. Geophys. Res., **89**, 11749-11757, https://doi.org/10.1029/JD089iD07p11749.

Jouzel, J., Russell, G. L., Suozzo, R. J., Koster, R. D., White, J. W. C., and Broecker, W. S. (1987). Simulation of the HDO and $H_2{}^{18}O$ Atmospheric Cycles Using the NASA GISS General Circulation Model: The Seasonal Cycle for Present-Day Conditions. J. Geophys. Res., **92**, 14739-14760, https://doi.org/10.1029/JD092iD12p14739.

Kurita, N., Noone, D., Risi, C., Schmidt, G. A., Yamada, H., and Yoneyama, K. (2011).

https://doi.org/10.5194/egusphere-2026-2351
Preprint. Discussion started: 20 May 2026

Intraseasonal isotopic variation associated with the Madden-Julian Oscillation. J. Geophys. Res., **116**, D24101, https://doi.org/10.1029/2010JD015209.

Lee, JE., and Fung, I. (2008). "Amount effect" of water isotopes and quantitative analysis of post-condensation processes. Hydrol. Process., **22**, 1-8, https://doi.org/10.1002/hyp.6637.

LeGrande, A. N., and Schmidt, G. A. (2006). Global gridded data set of the oxygen isotopic composition in seawater. Geophys. Res. Lett., **33**, L12604, https://doi.org/10.1029/2006GL026011.

Liu, Y., Gao, J., and Wang, Y. (2024). Evaluation of atmospheric moisture transport to the Tibetan Plateau from 33 CMIP6 models. npj Clim. Atmos. Sci., **7**, 231, https://doi.org/10.1038/s41612-024-00785-0.

Liu, Y., Gao, J., Werner, M., Cauquoin, A., and Li, K. (2026a). Observational data for evaluation, Figshare [data set], https://doi.org/10.6084/m9.figshare.31900747.

Liu, Y., Gao, J., Werner, M., Cauquoin, A., and Li, K. (2026b). Outputs from ECHAM6-wiso simulation at Kathmandu, Lulang, Muztag, and Namco, Figshare [data set], https://doi.org/10.6084/m9.figshare.31900705.

Liu, Y., Gao, J., Werner, M., Cauquoin, A., and Li, K. (2026c). Core representative analysis scripts used to evaluate model performance, Figshare [code], https://doi.org/10.6084/m9.figshare.31900777.

Mathieu, R., Pollard, D., Cole, J. E., White, J. W. C., Webb, R. S., and Thompson, S. L. (2002). Simulation of stable water isotope variations by the GENESIS GCM for modern conditions. J. Geophys. Res., **107**, ACL 2-1-ACL 2-18, https://doi.org/10.1029/2001JD900255.

Merlivat, L., and Jouzel, J. (1979). Global Climatic Interpretation of the Deuterium-Oxygen 18 Relationship for Precipitation. J. Geophys. Res., **84**, 5029-5033, https://doi.org/10.1029/JC084iC08p05029.

Nordeng, T. E. (1994). Extended versions of the convective parameterization scheme at ECMWF and their impact on the mean and transient activity of the model in the tropics. Tech. Rep., **206**, ECMWF, Reading, U. K.

Nusbaumer, J., Wong, T. E., Bardeen, C., and Noone, D. (2017). Evaluating

https://doi.org/10.5194/egusphere-2026-2351
Preprint. Discussion started: 20 May 2026

hydrological processes in the Community Atmosphere Model Version 5 (CAM5) using stable isotope ratios of water. J. Adv. Model. Earth Syst., **9**, 949-977, https://doi.org/10.1002/2016MS000839.

Ohmura, A., and Reeh, N. (1991). New precipitation and accumulation maps for Greenland. J. Glacial., **37**, 140-148.

Okazaki, A., and Yoshimura, K. (2019). Global Evaluation of Proxy System Models for Stable Water Isotopes With Realistic Atmospheric Forcing. J. Geophys. Res., **124**, 8972-8993, https://doi.org/10.1029/2018JD029463.

Putman, A. L., Feng, X., Sonder, L. J., and Posmentier, E. S. (2017). Annual variation in event-scale precipitation δ^2H at Barrow, AK, reflects vapor source region. Atmos. Chem. Phys., **17**, 4627-4639, https://doi.org/10.5194/acp-17-4627-2017.

Risi, C., Bony, S., Vimeux, F., and Jouzel, J. (2010). Water-stable isotopes in the LMDZ4 general circulation model: Model evaluation for present-day and past climates and applications to climatic interpretations of tropical isotopic records. J. Geophys. Res., **115**, D12118, https://doi.org/10.1029/2009JD013255.

Sarkar, M., Bailey, A., Blossey, P., de Szoeke, S. P., Noone, D., Quiñones Meléndez, E., Leandro, M. D., and Chuang, P. Y. (2023). Sub-cloud rain evaporation in the North Atlantic winter trade winds derived by pairing isotopic data with a bin-resolved microphysical model. Atmos. Chem. Phys., **23**, 12671-12690, https://doi.org/10.5194/acp-23-12671-2023.

Scherer, j. j., Paul, J. B., O'Keefe, A., and Saykally, R. J. (1997). Cavity ringdown laser absorption spectroscopy: History, development, and application to pulsed molecular beams. Chem. Rev., **97**, 25–52, https://doi.org/10.1021/cr930048d.

Shi, X., Risi, C., Li, L., Wang, X., Pu, T., Zhang, G., Zhang, Y., Wang, Z., and Kong, Y. (2022). What controls the skill of general circulation models to simulate the seasonal cycle in water isotopic composition in the Tibetan Plateau region? J. Geophys. Res., **127**, e2022JD037048, https://doi.org/10.1029/2022JD037048.

Steen-Larsen, H. C., Risi, C., Werner, M., Yoshimura, K., and Masson-Delmotte, V. (2016). Evaluating the skills of isotope-enabled general circulation models against in situ atmospheric water vapor isotope observations. J. Geophys. Res., **122**, 246-

https://doi.org/10.5194/egusphere-2026-2351
Preprint. Discussion started: 20 May 2026

263, https://doi.org/10.1002/2016JD025443.

Stevens, B., Giorgetta, M., Esch, M., Mauritsen, T., Crueger, T., Rast, S., Salzmann, M., Schmidt, H., Bader, J., Block, K., Brokopf, R., Fast, I., Kinne, S., Kornblueh, L., Lohmann, U., Pincus, R., Reichler, T., and Roeckner, E. (2013). Atmospheric component of the MPI-M Earth System Model: ECHAM6. J. Adv. Model. Earth Syst., **5**, 146-172, https://doi.org/10.1002/jame.20015.

Stewart, M. K. (1975). Stable Isotope Fractionation Due to Evaporation and Isotopic Exchange of Falling Waterdrops: Applications to Atmospheric Processes and Evaporation of Lakes. J. Geophys. Res., **80**, 1133-1146, https://doi.org/10.1029/JC080i009p01133.

Sturm, K., Hoffmann, G., Langmann, B., and Stichler, W. (2005). Simulation of delta O-18 in precipitation by the regional circulation model REMOiso. Hydrol. Process., **19**, 3425-3444, https://doi.org/10.1002/hyp.5979.

Sun, L., Yang, Y., Fu, Y., Zhang, X., Zhong, L., Zhao, C., and Ma, M. (2022). Summertime atmospheric water vapor transport between Tibetan Plateau and its surrounding regions during 1990-2019: Boundary discrepancy and interannual variation. Atmos. Res., **275**, 106237, https://doi.org/10.1016/j.atmosres.2022.106237.

Tan, M. (2013). Circulation effect: response of precipitation $\delta^{18}O$ to the ENSO cycle in monsoon regions of China. Clim. Dyn., **42**, 1067-1077, https://doi.org/10.1007/s00382-013-1732-x.

Tiedtke, M. (1989). A comprehensive mass flux scheme for cumulus parameterization in large-scale models. Mon. Weather Rev., **117**, 1779-1800, https://doi.org/10.1175/1520-0493(1989)117<1779:ACMFSF>2.0.CO;2.

Wang, X., Tolksdorf, V., Otto, M., and Scherer, D. (2021). WRF-based dynamical downscaling of ERA5 reanalysis data for High Mountain Asia: Towards a new version of the High Asia Refined analysis. Int. J. Climatol., **41**, 743–762, https://doi.org/10.1002/joc.6686.

Werner, M., Langebroek, P. M., Carlsen, T., Herold, M., and Lohmann, G. (2010). Stable water isotopes in the ECHAM5 general circulation model: Toward high-

https://doi.org/10.5194/egusphere-2026-2351
Preprint. Discussion started: 20 May 2026

resolution isotope modeling on a global scale. J. Geophys. Res., **116**, D15109, https://doi.org/10.1029/2011JD015681.

Wu, Z., and Huang, N. E. (2009). ENSEMBLE EMPIRICAL MODE DECOMPOSITION: A NOISE-ASSISTED DATA ANALYSIS METHOD. Adv. Data Sci. Adapt. Anal., **1**, 1-41, https://api.semanticscholar.org/CorpusID:207152935.

Xu, X., Lu, C., Shi, X., and Gao, S. (2008). World water tower: An atmospheric perspective. Geophys. Res. Lett., **35**, L20815, https://doi.org/10.1029/2008GL03586.

Yao, T., Masson-Delmotte, V., Gao, J., Yu, W., Yang, X., Risi, C., Sturm, C., Werner, M., Zhao, H., He, Y., Ren, W., Tian, L., Shi, C., and Hou, S. (2013). A review of climatic controls on $\delta^{18}O$ in precipitation over the Tibetan Plateau: Observations and simulations. Rev. Geophys., **51**, 525–548, https://doi.org/10.1002/rog.20023.

Yao, T., Thompson, L., Chen, D., and Piao, S. (2022). Reflections and future strategies for Third Pole Environment. Nat. Rev. Earth Environ., **3**, 608–610, https://doi.org/10.1038/s43017-022-00342-4.

Yoshimura, K., Miyazaki, S., Kanae, S., and Oki, T. (2006). Iso-MATSIRO, a land surface model that incorporates stable water isotopes. Global and Planetary Change, **51**, 90-107, https://doi.org/10.1016/j.gloplacha.2005.12.007.